

pubs.acs.org/JACS Article

# Reactive Chemical Environments Control Charge Carrier Selectivity and Photovoltage at Nanoparticle Electrocatalyst/Semiconductor Junctions in Solar Water Splitting

Ahmet Sert, Aarti Mathur, and Suljo Linic\*



Cite This: J. Am. Chem. Soc. 2025, 147, 30829-30841



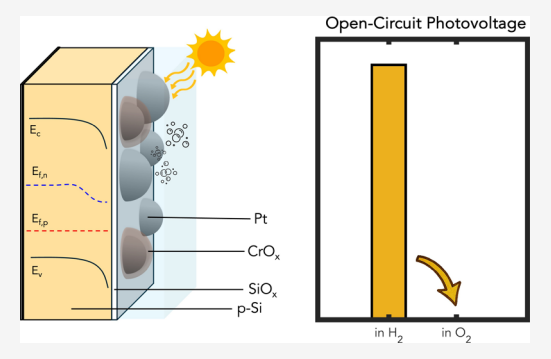
**ACCESS** I

III Metrics & More

Article Recommendations

Supporting Information

**ABSTRACT:** Interfacial charge transfer at electrocatalyst/semiconductor (EC/SC) junctions is central to the performance of photo(electro)catalysts, yet the influence of the reactive environment on these processes remains poorly understood. This is particularly the case for unburied EC/SC junctions, such as EC nanoparticles anchored on a SC (np-EC/SC), where reacting molecules readily access the EC surface sites and the np-EC/SC interfaces. Herein, we uncover a dynamic, chemically driven mechanism by which the local reaction environment modulates charge transfer at Pt/p-Si interfaces under solar water splitting conditions. We demonstrate that molecular adsorption of  $H_2$  and  $O_2$  at the metal/electrolyte interface induces interfacial dipoles on Pt nanoparticles, effectively tuning their work function and shifting the junction from Ohmic to rectifying behavior. This environment-responsive modulation of the Schottky



barrier height governs charge carrier selectivity independently of the commonly cited pinch-off effect, which is found to be negligible. Additionally, a spontaneously evolved thin  $SiO_x$  interlayer facilitates tunneling-mediated charge transfer while suppressing recombination, providing an additional degree of control over interfacial energetics. These findings reveal that catalytic surface chemistry can serve as a powerful lever for tuning electronic structure and photovoltage in nanoscale photoelectrode architectures, opening new design strategies for high-efficiency solar fuel systems.

### **■ INTRODUCTION**

Photo(electro) catalytic water splitting offers a promising route to clean and renewable hydrogen production. A widely studied approach couples metal nanoparticle electrocatalysts (np-ECs) with semiconductor (SC) light absorbers, where the SC harvests solar energy to generate charge carriers, which move to np-ECs that drive the hydrogen (HER) and oxygen (OER) evolution half-reactions.<sup>2-4</sup> Despite significant progress, the fundamental mechanisms governing charge transfer efficiencies (i.e., photovoltage) at np-EC/SC interfaces remain poorly understood, especially under reaction conditions.<sup>5</sup> The main reason for the limited understanding of these systems is that the np-EC/SC interfaces are highly complex and influenced by factors such as band alignment, interfacial charge transfer, and reaction-induced surface modifications. <sup>0-8</sup> Dynamic processes, such as light absorption, carrier generation, recombination, and electrolyte interactions can also impact the system behavior under operating conditions, further complicating the physical picture.9

As a result, even well-studied systems, such as Pt nanoparticles anchored on p-Si (np-Pt/p-Si) for the photo-electrochemical hydrogen evolution, 10-20 lack physical models that fully explain their significant performance gap when compared to their Pt thin-film (pf-Pt/p-Si) counterparts. One commonly proposed explanation for the discrepancy in

the behavior of np-EC/SC systems relative to their thin film EC on SC analogues is the *pinch-off* effect, which suggests that charge transfer at the np-EC/SC junction is not solely dictated by the catalyst and/or the semiconductor, but rather is controlled by the electrolyte environment that surrounds the EC nanoparticles. <sup>13,23–25</sup> In this view, external factors dominate interfacial charge transfer, to a large degree overriding the intrinsic properties of the np-EC/SC system. <sup>26,27</sup> However, the extent to which this effect governs functioning systems remains a topic of debate. <sup>3,8,28</sup> Additionally, direct exposure to the electrolyte can dynamically alter junction properties through surface oxidation, <sup>22,29,30</sup> catalyst redox transitions, <sup>31</sup> and hydrogen-induced modifications of the metal work function <sup>21,32</sup> -mechanisms that are in many cases not fully understood.

Unearthing how these interfacial interactions affect the performance of np-EC/SC photo(electro)catalysts is critical for designing more efficient solar water-splitting systems. In

Received: May 1, 2025 Revised: July 26, 2025 Accepted: August 11, 2025 Published: August 18, 2025





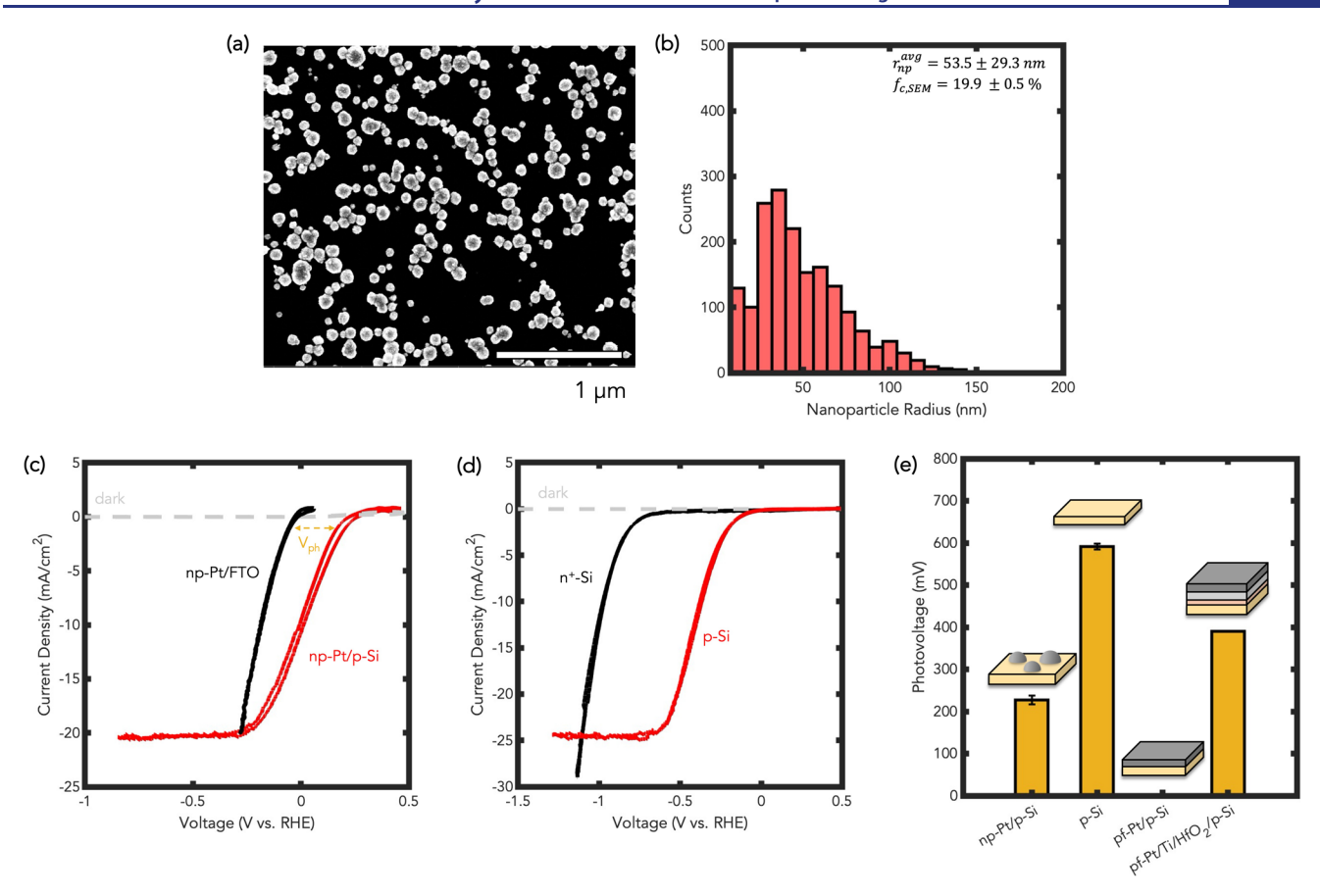


Figure 1. Characteristics and photoelectrochemistry of model Pt/p-Si systems. (a) SEM micrograph of the np-Pt/p-Si system. (b) Size distribution of Pt nanoparticles for the np-Pt/p-Si system. (c) CVs of np-Pt/p-Si and np-Pt/FTO ( $V_{\rm ph}$  shows an example photovoltage measured at 1 mA/cm<sup>2</sup>). (d) CVs of bare p-Si and n<sup>+</sup>-Si (e) Compiled experimental photovoltages at 1 mA/cm<sup>2</sup> of all systems. All CV data were collected in 0.1 M KOH saturated with  $H_2$  under 1-sun illumination at a scan rate of 50 mV s<sup>-1</sup>. For (e), the error bars are the s.d. values of measurements on at least three independent (n = 3) samples. The data are expressed as mean  $\pm$  s.d.

this study, we investigate how reaction environments influence charge transfer at np-EC/SC junctions, offering new insights into the fundamental physics that govern performance. Through a series of investigations of various Pt/p-Si model systems, we reveal that molecular adsorption processes involving H2 and O2 interactions with the EC play a decisive role in modulating charge transfer across the EC/SC junction. Our findings demonstrate that an initially nonselective (i.e., Ohmic) np-EC/SC contact can dynamically transform into one that is highly selective for the desired charge carrier (i.e., electrons) by simply altering the nature of the reactive environment that can access the EC. We further show that this physical model is sufficient to describe the measured photovoltage without the need of invoking the pinch-off effect. We quantitatively describe these findings through a comprehensive physical framework. Ultimately, these findings provide insight into design strategies that enable precise engineering of np-EC/SC junctions, offering avenues for optimizing the performance of practical solar water-splitting devices.

# ■ RESULTS AND DISCUSSION

We fabricated Pt nanoparticles on BHF-etched p-Si surfaces (denoted np-Pt/p-Si) through (photo)electrodeposition under simulated sunlight irradiation (see Figure S1 for details). We note that in aqueous solutions, the Si surface will oxidize, creating thin oxide layers with hydroxyl groups terminating the surface (see Figure S5 for the Pourbaix diagram of  $Si-H_2O$ ).

Figure 1a shows a representative high-magnification top-down scanning electron microscopy (SEM) image of a np-Pt/p-Si sample. Figure 1b shows the size-distribution of the Pt nanoparticles obtained from SEM images. The average Pt nanoparticle radius was  $53.5 \pm 29.3$  nm and the coverage of the surface (i.e., the fraction of the p-Si surface covered by Pt nanoparticles) was  $\approx 20\%$ . Additional SEM characterization can be found in Section S2.

The data in Figure 1c show the photoelectrochemical HER performance of the np-Pt/p-Si system under 1-sun illumination in 0.1 M KOH. As an electrocatalytic control, we fabricated Pt nanoparticles on a FTO support (np-Pt/FTO) using dark electrodeposition in the identical synthesis solution. The data in Figure 1c (black curve) show the dark electrochemical HER performance of np-Pt/FTO. We calculated the photovoltage of the system by comparing the onset potential (i.e., voltage at 1 mA/cm<sup>2</sup>) between the np-Pt/p-Si and np-Pt/FTO samples. This method assumes identical HER kinetics for the light and dark samples, and the measured photovoltage is the energy imparted on the EC by the illuminated SC while driving the electrochemical reaction (at a rate of 1 mA/cm<sup>2</sup>). The data in Figure 1c show that the np-Pt/p-Si system generates an average photovoltage of 227 ± 10 mV with a photolimiting current density of 20.3 mA/cm<sup>2</sup>.

To better understand the np-Pt/p-Si system, we fabricated and assessed the performance of several other model systems with different interface characteristics under identical testing

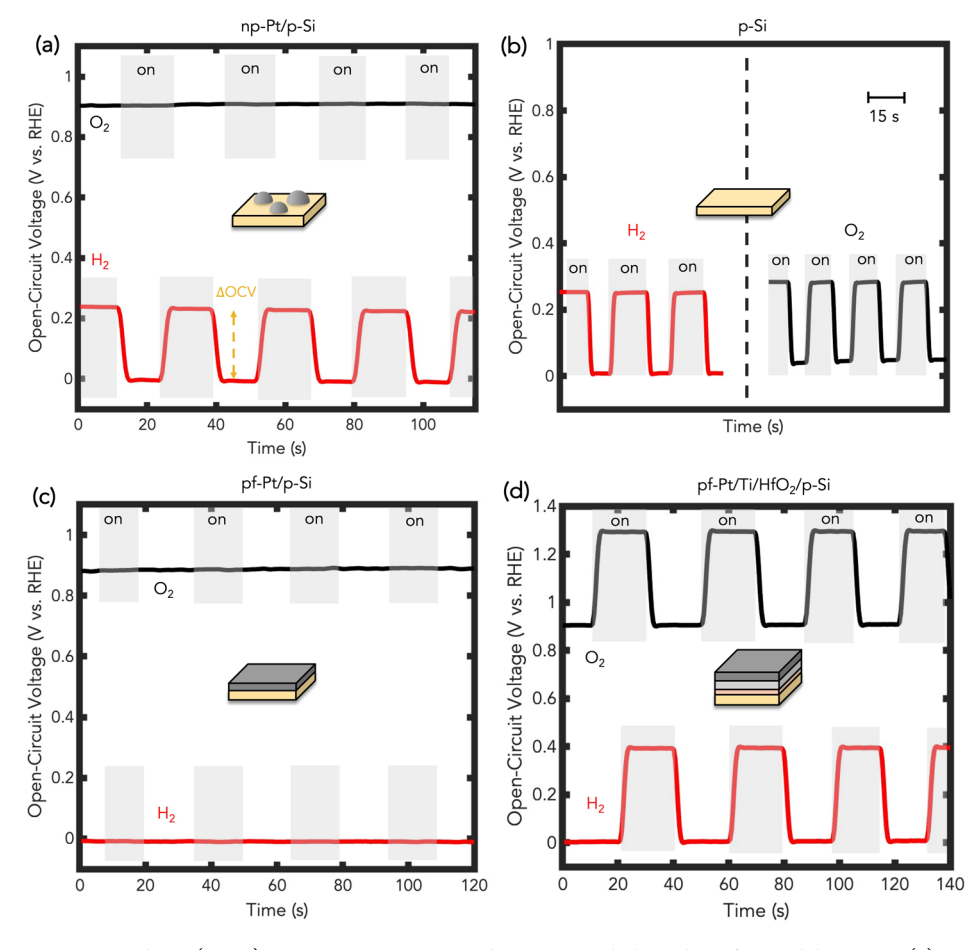


Figure 2. Transient open-circuit voltage (OCV) measurements in  $H_2$  and  $O_2$ -saturated electrolytes for model systems. (a) OCVs of (a) np-Pt/p-Si, (b) bare p-Si, (c) pf-Pt/p-Si and (d) pf-Pt/Ti/HfO2/p-Si.  $\Delta$ OCV is the shift in the OCV between light on (gray shaded areas) and off condition (i.e., open-circuit photovoltage). All data were collected in 0.1 M KOH under 1-sun illumination. See Figure S9 for the compilation of OCV data for all systems.

conditions. These included an etched bare p-Si sample with no catalyst (p-Si), a planar film of Pt on etched p-Si (pf-Pt/p-Si) as well as a planar film of Pt with a Ti interlayer on HfO2 covered p-Si (pf-Pt/Ti/HfO<sub>2</sub>/p-Si). The pf-Pt/Ti/HfO<sub>2</sub>/p-Si system is a typical metal-insulator-semiconductor (MIS) photoelectrode that we use as a model buried junction device. 33,34 The data in Figure 1d show the current densityvoltage behavior of p-Si and n<sup>+</sup>-Si systems for HER. The n<sup>+</sup>-Si system is used as a control to evaluate the photovoltage of p-Si, which we measure at 1 mA/cm<sup>2</sup>. The data show that bare p-Si generates a photovoltage of 591  $\pm$  7 mV, which is the highest photovoltage relative to the other systems. This high photovoltage is due to the high barrier height of the p-Si/ electrolyte junction and a low surface recombination velocity compared to metal contacts. 35,36 We note that bare p-Si also exhibits a higher photolimiting current density compared to np-Pt/p-Si due to the absence of parasitic light attenuation caused by Pt nanoparticles. 15 Our measurements also showed (see Figure S8) that pf-Pt/p-Si generates negligible photovoltage while pf-Pt/Ti/HfO2/p-Si generates a photovoltage of 390 mV, in agreement with our prior work.<sup>33</sup> Figure 1e shows the photovoltages measured under HER conditions for all four model systems.

We also investigated how these systems respond to changes in the electrolyte environment, specifically to  $H_2$  and  $O_2$  saturated electrolytes. We measured the open-circuit voltage

(OCV), which is the equilibrium potential of the electrode when no net current is flowing.<sup>37</sup> It has been established that the difference in the light and dark OCVs of photoelectrodes can serve as a measure of the open-circuit (OC) photovoltage generated by the system.<sup>38,39</sup> We note that the OC photovoltage measures the change in the quasi-Fermi level position of the majority charge carrier (i.e., holes in this case) in light-on and light-off states with no net current being generated.<sup>24,31,40</sup>

We purged the electrolyte with H<sub>2</sub> and O<sub>2</sub> and measured the OCV of photoelectrodes under light-on and light-off conditions. The data in Figure 2a show that in dark, the OCV of the np-Pt/p-Si system equilibrates to the surface electrochemical potential of Pt when in contact with aqueous electrolytes saturated with H2 or O2. The exact values of these potentials are dictated by the equilibrated elementary steps of the electrochemical reactions occurring on the Pt surface under a given set of reaction conditions. <sup>41</sup> In H<sub>2</sub>, the np-Pt/p-Si potential equilibrates to ~0 V vs RHE, corresponding to the redox potential of the reversible HER/HOR reactions on Pt. 42 On the other hand, in O<sub>2</sub>-rich aqueous solutions, the surface potential of Pt nanoparticles rests near the onset potential of oxygen reduction reaction (ORR) at ~0.9 V vs RHE. 24,43 Unlike the systems containing Pt EC, for bare p-Si, the potential of the surface does not move with respect to H2 and O2 and appears to be pinned near 0 V vs RHE (Figure

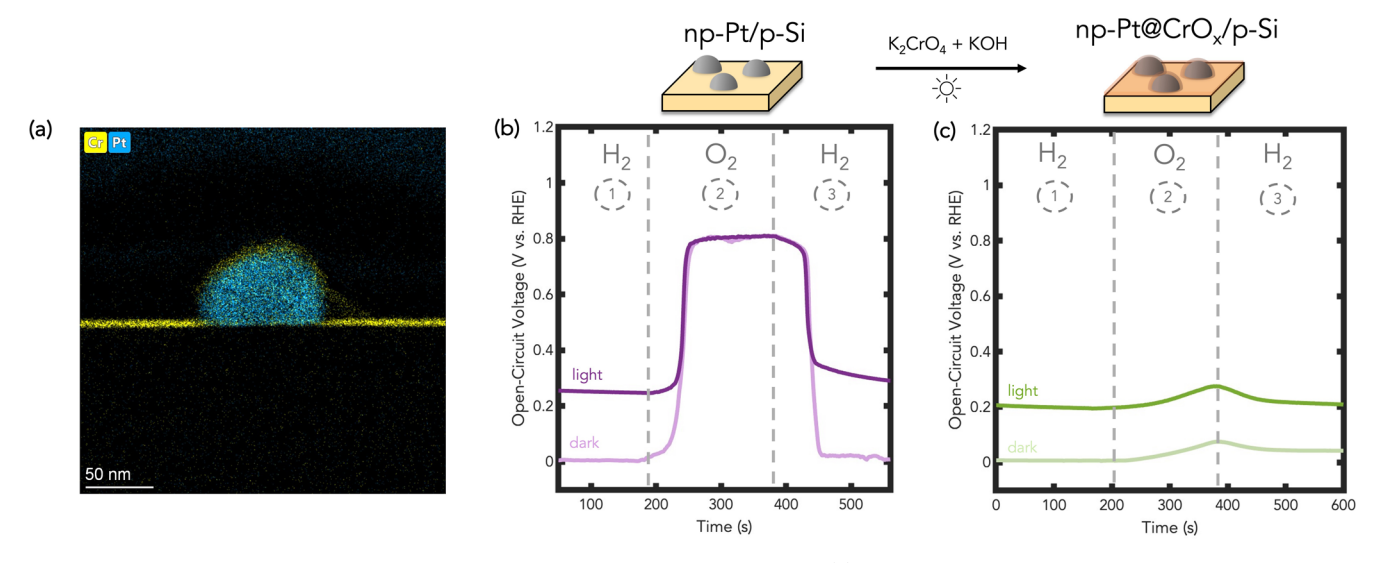


Figure 3. Modulating the local chemical environment of np-Pt/p-Si with  $CrO_x$  coating. (a) Cross-sectional STEM-EDS mapping of np-Pt@CrO<sub>x</sub>/p-Si. (b,c) Light and dark OCV responses to dynamic changes in the local chemical environment for (b) uncoated np-Pt/p-Si and (c) np-Pt@ $CrO_x$ /p-Si. All electrochemical data were collected in 0.1 M KOH under 1-sun illumination.

2b).  $^{44-47}$  We also measure that for pf-Pt/p-Si and pf-Pt/Ti/HfO<sub>2</sub>/p-Si systems, the OCVs in the dark equilibrate to the potential of the Pt EC in aqueous electrolytes saturated with H<sub>2</sub> or O<sub>2</sub>.

The data in Figure 2a show that the np-Pt/p-Si system generates a significant OC photovoltage of  $\sim\!230$  mV in the  $H_2$  environment, while in  $O_2$  it generates negligible OC photovoltage. The data in Figure 2b show that p-Si generates  $\sim\!250$  mV of OC photovoltage in both  $H_2$  and  $O_2$ . Moreover, Figure 2c show that pf-Pt/p-Si does not generate any OC photovoltage in  $H_2$  or  $O_2$ . Finally, the data in Figure 2d show that pf-Pt/Ti/HfO\_2/p-Si generates the same  $\sim\!390$  mV of OC photovoltage in both  $H_2$  and  $O_2$ . Overall, the data in Figure 2 show that for all systems other than np-Pt/p-Si, OC photovoltage does not show any sensitivity to changes in the local chemical environment.

The data in Figures 1 and 2 suggest several contradictions that cannot be explained using generally accepted, classical theories of photoelectrochemical interfaces. To describe these contradictions, we will first focus on the pf-Pt/Ti/HfO<sub>2</sub>/p-Si system which can be described using classical theories. The conventional theories (based on the simple Schottky model) suggest that the generated photovoltage of buried junctions (such as pf-Pt/Ti/HfO<sub>2</sub>/p-Si) in principle should not be affected by exposure to different local chemical environments. For example, in the pf-Pt/Ti/HfO<sub>2</sub>/p-Si system, the barrier height of the interface is mainly governed by the difference of the work functions of p-Si and the Ti interlayer which is completely screened from the electrolyte.<sup>33</sup> We note that here, the HfO2 insulator layer serves to decrease recombination by modulating the flux of charge carriers and prevents the deleterious effects of a direct metal/semiconductor contact (silicide formation, metal-induced gap states, etc.). The fact that the OC photovoltage of the pf-Pt/Ti/HfO<sub>2</sub>/p-Si system does not exhibit such changes in H<sub>2</sub> and O<sub>2</sub> (Figure 2d) is consistent with this classical model.

Similar to the pf-Pt/Ti/HfO<sub>2</sub>/p-Si system, one would expect that band bending in systems where Pt and Si are in direct contact should be governed by the difference of the work functions of p-Si and the Pt. Intrinsically, the Fermi level of Pt

(set by its work function of 5.12-5.93 eV) is approximately aligned with the Fermi level of p-Si ( $\sim$ 5 eV in our case) (we note that this gets more complicated as we describe further below). According to the simple Schottky model, the Pt/p-Si interface should thus form an Ohmic contact with no photovoltage. The data for pf-Pt/p-Si seems to support this argument since no photovoltage is generated in H<sub>2</sub> or O<sub>2</sub>. In contradiction, the np-Pt/p-Si system generates significant photovoltage in H<sub>2</sub> and none in O<sub>2</sub>. Therefore, conventional Schottky theory fails to explain the source of photovoltage in H<sub>2</sub> for this system.

In general, one can work around this issue by invoking the pinch-off effect, which would suggest that the electrolyte potential can dictate the barrier height at the interface of the SC and the electrolyte. In this case, the p-Si/electrolyte junction could "pinch off" the np-EC/SC junction by creating an effective barrier height. 19,24 However, for this to be applicable, there needs to be a different barrier height between the electrolyte and the SC in H<sub>2</sub> and O<sub>2</sub>-rich environments, in addition to having sufficiently small metal nanoparticles to be in the pinch-off regime (we will discuss the latter requirement below). The problem is that this does not seem likely since the data in Figure 2b show that the p-Si system generates identical photovoltage under H<sub>2</sub> and O<sub>2</sub>-rich conditions. As postulated above, p-Si in aqueous electrolytes is known to exhibit Fermi level pinning that governs the generated photovoltage. Simply put, p-Si/electrolyte band energies do not communicate with  $H_2$  or  $O_2$  in the electrolyte.<sup>45,49</sup>

The data in Figure 2 illustrate that in the case of the np-Pt/p-Si system, the reaction environment has a large influence on charge transfer between the EC and SC and therefore the photovoltage generated by the system, and that the pinch-off effect alone is unable to account for this behavior. To further test this hypothesis that the interface between the electrolyte and the SC (i.e., electrolyte-induced pinch-off effect) does not govern the photovoltage changes in np-Pt/p-Si in H<sub>2</sub>- versus O<sub>2</sub>-rich electrolytes, we fabricated a model system that allows us to decouple the reaction environment of the SC/electrolyte interface from that of the EC/electrolyte interface. For this purpose, we used a CrO<sub>x</sub> membrane to coat the surface of Pt

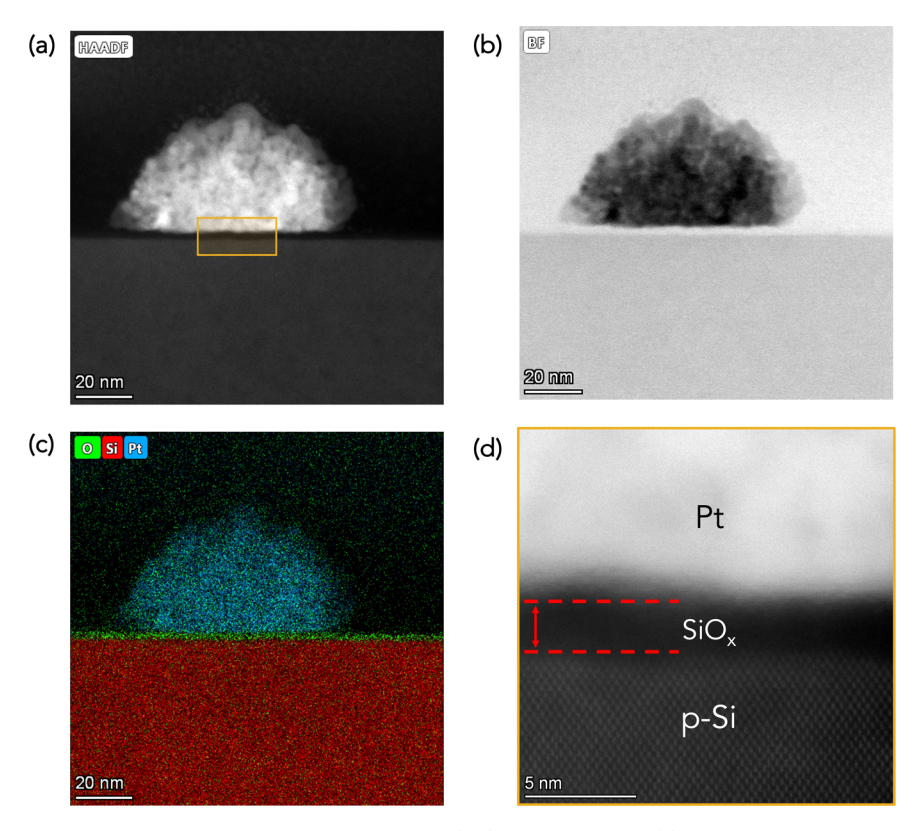


**Figure 4.** Ex-situ atomistic characterization of the np-Pt/p-Si interface. (a,b) Cross-sectional (a) high-angle annular dark field (HAADF) and (b) bright field (BF) STEM image of a Pt nanoparticle resting on p-Si after electrochemical testing. (c) EDS elemental mapping of np-Pt/p-Si. (d) HR-HAADF-STEM image of the np-Pt/Si interface. Red dashed line highlights the boundaries of the interfacial SiO<sub>x</sub> layer. See **Figure S4** for additional STEM images.

EC nanoparticles. In water-based electrolytes, these materials are present in the form of hydrated metal oxide shells  $(CrO_{(1.5-m)}(OH)_{2m}\cdot xH_2O)$  in this case) that selectively block the transport of  $O_2$  through the membrane while allowing the transport of water and  $H_2$ . To fabricate these systems, we (photo)electrodeposited thin layers of  $CrO_x$  on the np-Pt/p-Si system (Figure S10). Figure 3a shows the cross-sectional STEM-EDS mapping of the np-Pt@ $CrO_x$ /p-Si system, which confirms that thin layers of Cr (approximately 3–5 nm in thickness) are covering the Pt nanoparticles (see also Figure S12).

The data in Figure 3b,c show the light and dark OCVs for the uncoated np-Pt/p-Si and coated np-Pt@CrOx/p-Si systems, respectively in response to dynamic changes in the electrolyte, going from a H2- to O2-rich electrolyte. Initially, the electrolyte was continuously saturated with  $H_2$  (region 1), subsequently O<sub>2</sub> was introduced to the cell and both H<sub>2</sub> and  $O_2$  were cofed at the same flow rate (region 2), and finally  $O_2$ flow was cut off while H<sub>2</sub> kept on flowing (region 3). We observe that for both systems, np-Pt/p-Si and np-Pt@CrO<sub>x</sub>/p-Si, the SC potential in the H<sub>2</sub>-rich electrolyte equilibrates to ~0 V vs RHE in dark. The data in Figure 3b show that for the uncoated np-Pt/p-Si system, the presence of O2 in the electrolyte shifts the potential in the dark to be closer to the potential of Pt in  $O_2$ . Consistent with the data in Figure 2, the OC photovoltage (measured by the difference of light on and off voltages) is generated under H2, but is not observed after O2 is introduced. On the contrary, the data in Figure 3c show that for np-Pt@CrOx/p-Si, the presence of O2 has minimal impact on the voltage in light and dark. We observe that this voltage is almost entirely controlled by the  $H_2O/H_2$  redox

couple, with small and delayed positive shifts observed over the course of ~200 s in the  $O_2$  electrolyte. We also observe in Figure 3c that the OC photovoltage is generated by the coated np-Pt@CrO<sub>x</sub>/p-Si system in an electrolyte where  $O_2$  and  $H_2$  coexist, comparable in magnitude to that generated by the uncoated np-Pt/p-Si system in just  $H_2$ . These data show that the CrO<sub>x</sub> shell maintains the system photovoltage even in the presence of  $O_2$ .

We also performed control experiments with p-Si/CrO $_x$  junctions (see Figure S11) and saw that these samples behaved qualitatively similar to bare p-Si. Importantly, in line with the behavior of the p-Si/electrolyte junction, the dark OCV and the generated OC photovoltage do not seem to respond to  $\rm H_2$  and  $\rm O_2$  in the electrolyte environment. This shows that the p-Si/CrO $_x$  interface cannot account for the behavior we observe in these systems (Figure 3c).

The results in Figure 3 provide further evidence that the pinch-off effect does not play an important role in the np-Pt/p-Si system, as the varying local chemical environment of the Pt EC exclusively controls the photovoltage of the np-EC/SC junction. In other words, p-Si/electrolyte junction energetics (which behave similarly in the cases with and without the  $CrO_x$  coating) do not influence charge transfer through the np-EC/SC contact. This is evidenced by the fact that the only function of  $CrO_x$  is to modulate the local environment of the Pt EC by selectively blocking the diffusive transfer of  $O_2$  to the surface of the EC from the electrolyte. We hypothesize that the underlying physical mechanism for this behavior involves the adsorption/desorption of  $H_2$  and  $O_2$  on the surface of Pt and at the Pt/p-Si interface. These adsorption processes at the EC/SC interface could lead to changes in the effective work

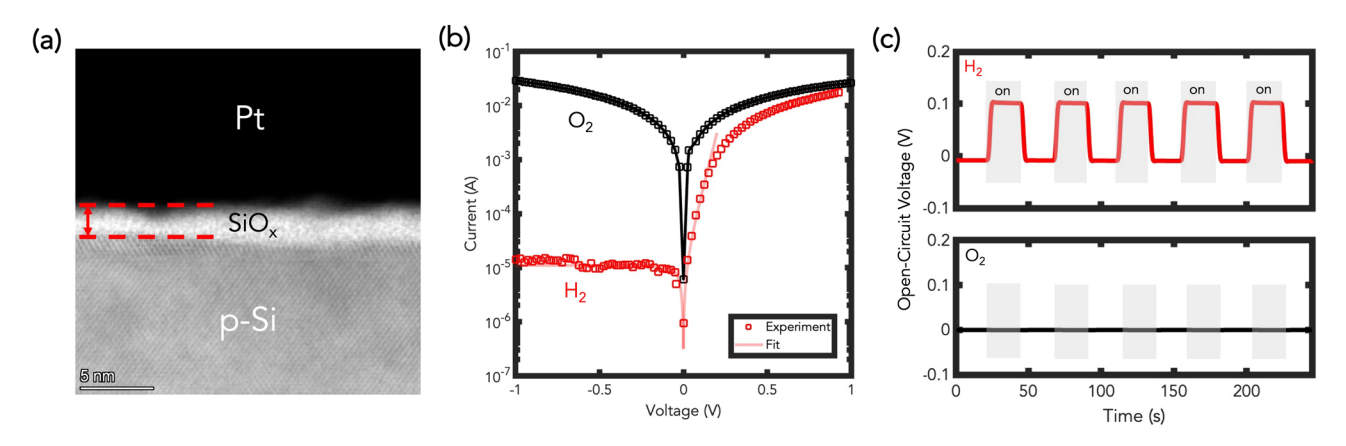


Figure 5. Solid-state electrical characterization of the  $Pt/SiO_x/p$ -Si interface. (a) Cross-sectional BF-STEM image of the  $St-Pt/SiO_x/p$ -Si sample. Red dashed lines highlight the boundaries of the  $SiO_x$  layer. See Figure S7 for additional STEM images. (b) Dry solid-state I–V measurements of  $St-Pt/SiO_x/p$ -Si under continuous flow of  $St-Pt/SiO_x/p$ -Si under continuous flow of  $St-Pt/SiO_x/p$ -Si in  $St-Pt/SiO_x/p$ -Si in St-Pt/Si

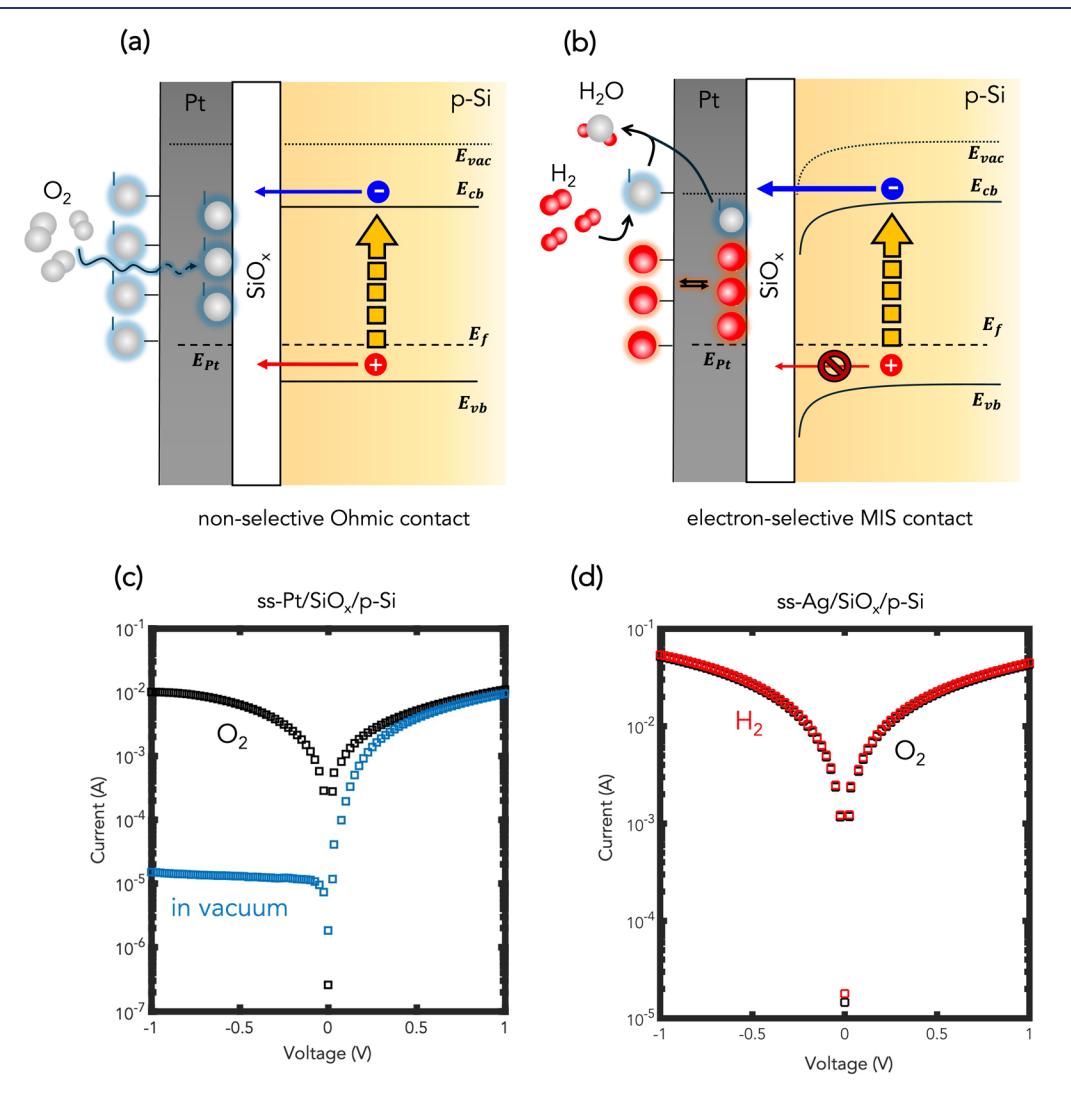


Figure 6. Mechanisms for dipole-mediated barrier formation. (a)  $O_2$  adsorption and diffusion leads to  $O_{ad}$  on the Pt surface and the  $Pt/SiO_x$  interface with partial electronegative charge, which increases the effective work function and leads to the experimentally observed nonselective Ohmic behavior. (b)  $H_2$  spontaneously reacts with  $O_{ad}$  to form water, cleans the surface and the interface and neutralizes the negative dipole. As a result, the effective work function decreases, leading to band bending with substantial barrier and electron-selectivity.  $E_{vao}$   $E_{cb}$ ,  $E_{vb}$ ,  $E_{f,p}$ , and  $E_{f,pt}$  are the vacuum energy, conduction band edge, valence band edge, Fermi level of p-Si and Fermi level of Pt, respectively. (c,d) Dry solid-state I–V measurements of a (c) ss-Pt/SiO<sub>x</sub>/p-Si sample in vacuum and when re-exposed to  $O_2$ , and (d) ss-Ag/SiO<sub>x</sub>/p-Si system under continuous flow of  $H_2$  or  $O_2$ . Scan rate was 100 mV s<sup>-1</sup>. The band diagrams are not drawn to scale.

function and consequently, the barrier height of the interface. <sup>21,22,53</sup>

To test this hypothesis and shed light on this unique behavior of np-Pt/p-Si systems, we characterized the np-Pt/p-Si interface using cross-sectional scanning transmission electron microscopy (STEM). Figure 4a,b shows STEM images of a representative Pt EC nanoparticle resting on the surface of p-Si. Energy-dispersive X-ray spectroscopy (EDS) mapping in Figure 4c confirms the presence of Pt and Si. Figure 4c also shows that there is a strong O signal coming from the surface of p-Si and the interface with Pt. Figure 4d shows a high-resolution STEM image of the interface and reveals a thin interfacial SiO<sub>x</sub> layer under the Pt nanoparticle. The observed formation of  $SiO_x$  on the p-Si surface is inevitable due to its chemical instability in the electrolyte, even under reducing potentials (see Section S8 for a discussion of possible mechanisms for the formation of this oxide). We measured the thickness of this interfacial oxide layer from multiple points across the sample to be 2.38  $\pm$  0.25 nm. The consequence of having the interfacial SiO<sub>x</sub> is that the charge carriers need to tunnel through this insulator to reach the Pt nanoparticle.<sup>54</sup> In this case, the np-Pt/p-Si interface resembles a metal-insulator-semiconductor (MIS) junction, and the impact of the insulating layer needs to be included for a complete quantitative analysis.6

To interrogate the electrical properties of the Pt/SiO<sub>x</sub>/p-Si junction and its response to the local chemical environment without the presence of electrolyte, we performed solid-state electrical characterization under dry conditions on systems that closely resemble those used in the electrochemical studies (shown in Figure 4). For this purpose, a ~40 nm thick film of Pt was electron-beam evaporated onto a chemically oxidized SiO<sub>x</sub>/p-Si sample (denoted ss-Pt/SiO<sub>x</sub>/p-Si where ss- stands for solid-state) (see Methods for fabrication details). Figure 5a shows the STEM cross-section of the sample with well-defined boundaries between different layers. The thickness of the SiO<sub>x</sub> layer of this sample was measured to be  $2.3 \pm 0.29$  nm, similar to the np-Pt/p-Si samples. We expect the nature of the  $SiO_x$ layer for np-Pt/p-Si and ss-Pt/SiO<sub>x</sub>/p-Si samples to also be similar since both SiO<sub>x</sub> layers were chemically oxidized in a self-limited manner. EDS mapping confirmed the chemical composition of the ss-Pt/SiO<sub>x</sub>/p-Si system (see Figure S6).

We used dry current-voltage (I-V) measurements under continuous flow of H2 and O2 gases to understand the impact of the local chemical environment on the junction characteristics of the Pt/SiO<sub>x</sub> interface. Data in Figure 5b show the dry I-V behavior of the ss-Pt/SiO<sub>x</sub>/p-Si system in H<sub>2</sub> and O<sub>2</sub> environments. The data show that in  $O_2$ , the system exhibits Ohmic behavior with no barrier as evidenced by the symmetric I-V curve (black data points). On the contrary, the data show that in H2, the system shows asymmetric I-V behavior, resembling a MIS Schottky diode with a significant barrier height (red data points).<sup>48</sup> The response of the system to switching between H2 and O2-rich environments is fast and fully reversible (see Figure S18). To test whether this H<sub>2</sub>induced barrier can be converted into useful photovoltage, we performed dry OCV measurements under broadband illumination. The data in Figure 5c show that the ss-Pt/SiO<sub>x</sub>/p-Si junction generates significant open-circuit photovoltage (~100 mV) in H<sub>2</sub> while it does not generate any in O<sub>2</sub> (see Section S17 for the electrochemical assessment of this architecture). This behavior is consistent with the photoelectrochemical

photovoltage trends shown in Figure 3a for np-Pt/SiO $_x$ /p-Si junctions.

The results in Figure 5 establish that the  $Pt/SiO_x/p$ -Si junction experiences significant changes in the interface barrier height upon exposures to  $H_2$  and  $O_2$ , even under dry conditions without the electrolyte present. In  $O_2$ , the junction behaves as Ohmic (i.e., no barrier, nonselective) (Figure 6a) while in  $H_2$ , it has a moderate barrier height and favors the selective transfer of electrons over holes (Figure 6b).

We hypothesize that these changes are caused by surface and interface dipoles induced by the dissociative adsorption and diffusion of  $H_2$  and  $O_2$  on Pt. It is known that adsorption of molecular or atomic species can lead to changes in the work function of metal surfaces due to adsorbate-induced dipole moments. For example, metallic polycrystalline Pt can readily dissociate  $O_2$  into monatomic  $O_{ad}$ . Due to the electronegativity of the O atoms, this leads to the creation of an electric dipole associated with the Pt–O bond, leading to an increase in the work function of Pt.  $^{57-61}$ 

The picture that emerges, based on the results discussed above, is that the work function of the Pt surface with adsorbed O atoms creates an Ohmic contact to the  $\mathrm{SiO}_x/\mathrm{p}\text{-Si}$  interface. This is why we do not observe any photovoltage in the presence of  $\mathrm{O}_2$  when Pt is covered by atomic O. On the other hand, Pt is known to dissociate  $\mathrm{H}_2$  rapidly to atomic  $\mathrm{H}_{\mathrm{ad}}$  with a high sticking probability. Had can spontaneously react with  $\mathrm{O}_{\mathrm{ad}}$  on the surface to form water and replace the Pt—O bond with Pt—H bonds. Had adsorption of the H atoms on a clean Pt surface has no dipole since the Pt—H bond is short and any charge on the H atoms is well shielded by the Pt electron density associated with the topmost Pt layers. This picture is supported by previous reports which reported that the adsorption of  $\mathrm{H}_2$  on Pt removes adsorbed O atoms, leading to a decrease in the work function.  $\mathrm{^{56,63,65}}$ 

We note that for the junction barrier height to be affected by the changes in the work function of Pt, the reactions between O2, H2 and Pt need to occur at the Pt/SiOx interface. The question is how these atoms reach the interface, particularly in the solid-state measurements, where the Pt film thicknesses were ~40 nm. It has been shown that thin films of Pt with thicknesses less than 100 nm can rapidly diffuse atomic H<sub>ad</sub>. 66,67 Furthermore, it has been reported that molecular O<sub>2</sub> can also diffuse through evaporated films of Pt. 68,69 This is because evaporated Pt films, by nature, consist of a continuous layer of nanoparticles with grain boundaries large enough for  $O_2$  to diffuse. Therefore, it is very likely that  $H_{ad}$  and  $O_{ad}$  can reach the Pt/SiO<sub>x</sub> interface leading to the observed changes in the junction barrier height (see Section \$16 for a discussion of alternative mechanisms). We also note that electrodeposited Pt nanoparticles appear corrugated and could further enable the access of molecular species in the chemical environment to the interface.

To test this hypothesis directly, we performed solid-state measurements on a ss-Pt/SiO $_{\rm x}$ /p-Si sample in a O $_{\rm 2}$ -free environment. For this purpose, the fabricated sample was promptly moved to a N $_{\rm 2}$ -purged glovebox and was vacuum evacuated for 7 days. We expect that most of the O $_{\rm ad}$  on the surface of Pt and the interface will desorb under these conditions. The data in Figure 6c show that the I–V behavior of the system in vacuum (with no O $_{\rm 2}$  or H $_{\rm 2}$  in the environment) is qualitatively very similar to when the sample is exposed to H $_{\rm 2}$  under ambient conditions (Figure 5b). When the sample was taken out of the glovebox and exposed to air

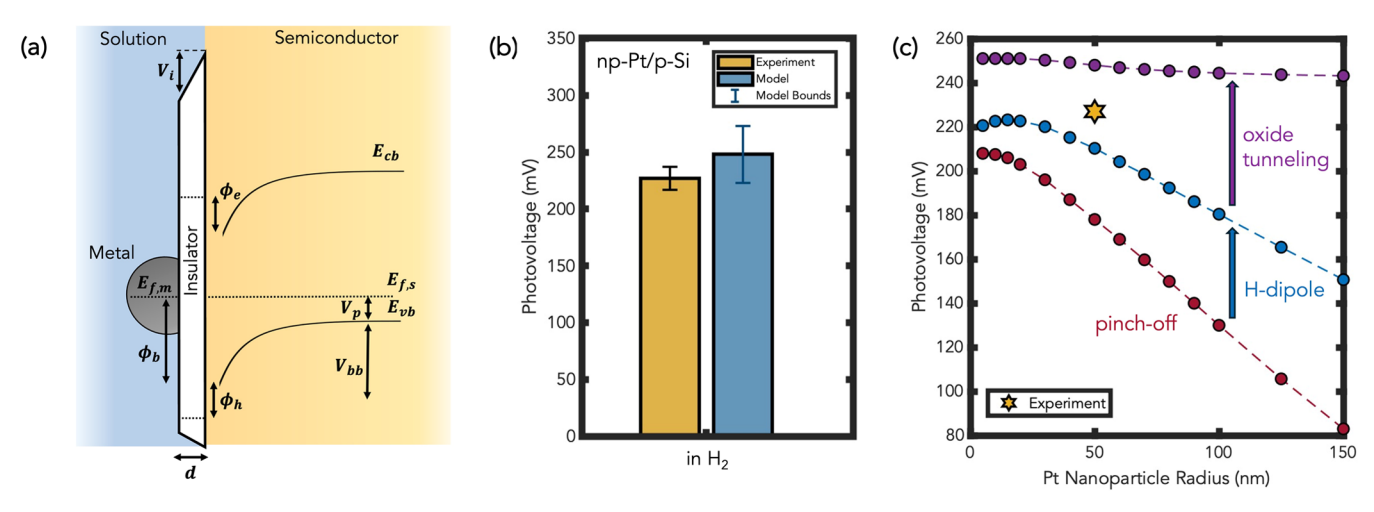


Figure 7. Computational model domain and results. (a) Energy band diagram in equilibrium depicting relevant bulk and interfacial variables for the modeled nanoparticle metal—insulator-semiconductor (np-MIS) junction.  $E_{\rm cb}$ ,  $E_{\rm vb}$ ,  $E_{\rm f,s}$ ,  $V_{\rm p}$  and  $V_{\rm bb}$  are the conduction band edge, valence band edge, Fermi level, distance of Fermi level to the valence band edge and band bending in the semiconductor, respectively.  $\phi_{\rm e}$ ,  $\phi_{\rm h}$ , d,  $V_{\rm i}$ ,  $E_{\rm f,m}$  and  $\phi_{\rm b}$  are the tunneling barrier for electrons, tunneling barrier for holes, thickness of the insulator layer, voltage drop through the interface, Fermi level of the metal, and the barrier height, respectively. Not drawn to scale. (b) Modeled photovoltages for the np-Pt/p-Si system and its comparison to the experimental photovoltage in  $H_2$ . Model bounds include uncertainty on the experimentally measured variables that serve as inputs to the model. Baseline model parameters can be found in the Table S4. (c) Modeled photovoltages as a function of nanoparticle size at constant coverage of 20% for the np-Pt/p-Si system showing the theoretical impact of pinch-off, H-induced interface dipole and oxide tunneling. All photovoltages were calculated at open-circuit (i.e., zero current).

for several hours, it went from being rectifying to Ohmic again. This result unambiguously demonstrates that  $O_{ad}$  induced dipoles play an important role in dictating the barrier height of the junction.

According to the mechanism presented above, it is evident that changes in the interface dipole moment should be governed by the interactions of the metal EC with  $O_2$  and  $H_2$ . To validate this hypothesis further, we tested the same system with a different metal (in place of Pt) that is known to be inert toward  $H_2$ , specifically Ag (denoted as ss-Ag/SiO<sub>x</sub>/p-Si). It is well-known that Ag has a similar work function to Pt, it can adsorb and dissociate  $O_2$ , while it does not interact with  $H_2$ . The data in Figure 6d show that the Ag system shows Ohmic behavior in  $O_2$ , and it does not show any sensitivity to  $H_2$ . This result is consistent with the reactivity of Ag toward  $H_2$  dissociation at room temperature and pressure.

Finally, to quantitatively describe how the mechanisms outlined above impact the photovoltage, we developed a finite-element based model to describe the behavior of np-Pt/p-Si. We first utilized solid-state measurements to extract interfacial parameters for the fabricated Pt/SiO<sub>x</sub> junction that are otherwise not known. We fit the I–V data of ss-Pt/SiO<sub>x</sub>/p-Si in H<sub>2</sub> to the diode equation (the fit is shown in Figure 5b) to extract the ideality factor (n) and the reverse saturation current ( $I_s$ ). The extracted average values were 1.45 and 1.83 × 10<sup>-5</sup> A, respectively. The measured ideality factor greater than 1 in this system is a manifestation of nonidealities and defects at the MIS junction which lead to a voltage drop across the interface (see Section S14 for a detailed discussion).<sup>73</sup>

To evaluate the Schottky barrier height  $(\phi_b)$  of the system in  $H_2$  and  $O_2$  environments, we used solid-state impedance spectroscopy. The impedance data can be fit to the Mott–Schottky equation to determine the ideal barrier height  $(\phi_{b,ideal})$ . We note that this barrier height is free from the influence of nonidealities as it is measured through the flatband potential, which is the potential at which the interface states are not charged. Figure S15 shows the Mott–Schottky

plot of the ss-Pt/SiO<sub>x</sub>/p-Si system under H<sub>2</sub>. We note that Mott—Schottky measurements could not be performed in O<sub>2</sub> since the system is Ohmic with no barrier, which is a limitation commonly observed. The slope and the intercept of the linear fit of the Mott—Schottky plot (red dashed line) is used to obtain the p-Si acceptor doping density ( $N_A$ ) and the flat band potential ( $V_{fb}$ ), respectively (see Supporting Information for an example analysis). With  $\phi_{b,ideal}$  n and  $I_s$  known, the actual barrier height ( $\phi_b$ ) and the insulator interfacial properties can also be quantified. The calculated values are in the expected range for similar SiO<sub>x</sub> layers at nanoscale (see Supporting Information for methodology and list of extracted experimental parameters).  $^{3,28}$ 

We built a model of the np-Pt/p-Si system to analyze how the mechanisms discussed above impact its performance. Input parameters to the model describing the Pt/SiO<sub>x</sub> interface were measured experimentally, as described above (see Table S4 for a list of model parameters). A detailed description of the model and the theory is provided in the Supporting Information. In short, we used the COMSOL finite element solver to numerically solve the governing semiconductor equations (i.e., Poisson's, drift-diffusion, continuity, etc.) in a 2D cylindrical coordinate system to calculate the potential and charge carrier concentration profiles for an illuminated SC. The boundary conditions of the model are illustrated in Figure S21. The 2D axisymmetric geometry allows to capture the impact of the geometric size and the reduced contact area of the EC, as well as the possible impact of the pinch-off effect by the surrounding electrolyte periphery. The model also includes contributions from nonidealities and tunneling through the interfacial oxide for both charge carriers (i.e., electrons and holes).<sup>54</sup> Relevant bulk and interface parameters are depicted in the band diagram shown in Figure 7a.

The data in Figure 7b show the modeled photovoltage in  $\rm H_2$  compared to the experimentally measured photovoltage for the np-Pt/p-Si system excluding the electrolyte-induced pinch-off effect. The data show that the model results are in good

agreement with the experimental data. The modeled photovoltage is shown within a confidence interval based on the uncertainty of experimentally measured interfacial parameters (Table S4). We note that in O2, both modeled and measured photovoltages are negligible due to the Ohmic nature of the contact.

We also explored the possible impact of the electrolyteinduced pinch-off effect on the performance of np-Pt/p-Si using the computational model, in addition to our detailed experimental assessment earlier. We assumed the p-Si/ electrolyte junction barrier height  $(\phi_{b,el})$  to be 0.73 eV, following assumptions from prior studies. <sup>13,23</sup> A sensitivity analysis for variations in  $\phi_{b,cl}$  can be found in Figure S24. The data in Figure 7c show the modeled photovoltages as a function of the Pt nanoparticle size at a constant Pt coverage on p-Si of 20%. We first modeled the case assuming electrolyte-induced pinch-off as the only mechanism leading to barrier formation in the system (red data points). The np-Pt/p-Si contact was assumed to be Ohmic in this case (this is consistent with O2 adsorbed on Pt surface). The red data points in Figure 7c show that the photovoltage shows sizedependence (see also Figures S22 and S23), consistent with the pinch-off theory (assuming none of the other mechanisms discussed above play a role). Interestingly, in the experimentally relevant size range (i.e., 50 nm radius), the model significantly underpredicts the experimental photovoltage measured in H<sub>2</sub>. Additionally, the model predicts photovoltage generation due to pinch-off in O2 while experimentally, we did not observe any photovoltage when the system was exposed to O<sub>2</sub> (see Figure 2a). These results show that the pinch-off effect alone falls short of describing the system behavior.

To explore this phenomenon further, we introduced a dipole-mediated barrier height (consistent with the H<sub>2</sub>-induced removal of O2 from the Pt surface which we explored above in this text) to the model in combination with the pinch-off effect assuming an ideality factor of unity (blue data points). The data show that in this scenario, the modeled photovoltages are higher and closer to the experimentally measured photovoltage. Note that a strong size dependence still exists in this case. Based on this data alone, one could think that the pinchoff effect and the dipole-mediated barriers can describe the np-Pt/p-Si system. However, as we demonstrated above, a SiO<sub>x</sub> tunnel oxide exists between Pt and p-Si, and its impact needs to be included as well. When oxide tunneling and nonidealities are added to the model (purple data points), the photovoltage increases further, but this photovoltage is not dependent on the Pt nanoparticle size anymore. These results show that in the case when all relevant mechanisms are included (i.e., barrier due to dipoles, oxide tunneling, nonidealities) the impact of the pinch-off effect is reduced to a negligible level of a 6 mV improvement for a 50 nm radius nanoparticle compared to the case without pinch-off (Figure 7b). Taken together, this analysis shows that it is not necessary to invoke the pinch-off effect to explain the performance of the np-Pt/p-Si system and doing so could lead to inconsistencies in the interpretation of experimental findings. These findings thus support the experimental analysis we have presented above.

Collectively, our modeling and experimental results reveal how a synergy of mechanisms is fundamentally required for even the seemingly simple np-Pt/p-Si junction to selectively collect the desired charge carrier (i.e., electrons) over the undesired (i.e., holes) and lead to the generation of photovoltage. Our findings indicate that H<sub>2</sub> in the local

chemical environment and its interaction with O<sub>2</sub> on Pt plays a decisive role in setting the barrier height of the junction through surface and interface dipoles. However, this barrier is not the only factor leading to the electrochemically observed photovoltages. This is because the H-induced barrier is moderate and would lead to a negligible photovoltage in a direct metal/semiconductor contact. The magnitude of this barrier is set by the dipole strength of adsorbates on Pt under these temperature and pressure conditions. 56

The interfacial SiO<sub>x</sub> formed in situ helps the system take full advantage of the local chemical environment induced barrier by imposing a tunneling barrier on the charge carrier fluxes, thus decreasing the accumulation of undesired holes (i.e., recombination current). However, it also introduces defect states (i.e., nonidealities) at the interface and compromises a portion of this energetic barrier. We note that the interfacial SiO<sub>x</sub> also acts as a diffusion barrier to prevent silicide formation (Figure S19a), which otherwise leads to deleterious Fermi level pinning caused by metal induced gap states. This is evidenced by the solid-state measurement results on ss-Pt/p-Si system (Figure S19b), which show that the system does not have any sensitivity to  $H_2$ . In other words, the presence of  $SiO_r$ allows the Fermi level of the junction to respond to the local chemical environment induced changes in the effective work function of Pt.

Finally, it is important to contextualize our findings described above in relation to other works. Previous reports have identified shifts in the effective work function and barrier height of Pt-group metal contacts to various SCs under H<sub>2</sub>, attributing these changes to dipoles from adsorbed H.32,53,7 These studies: however, did not directly examine these effects in a functioning photoelectrochemical system or explore this and other mechanisms (e.g., the role of interfacial oxides) in detail. Our extensive analysis of the prototypical np-Pt/p-Si system addresses these gaps by considering the mechanistic pathways through which adsorbates influence the system. We show that H2 itself does not impose a dipole directly but instead removes adsorbed O species, which we show are responsible for a strong electronegative dipole and the resulting high work function and Ohmic contact behavior. We also show that to completely explain the system, it is necessary to account for the role of interfacial oxides spontaneously formed between the Si SC and EC under relevant reaction conditions.

## CONCLUSIONS

In conclusion, we explored how local chemical environments of metal electrocatalysts modulate charge transfer across nanoscale EC/SC junctions. We demonstrated through a case study of a Pt nanoparticle/p-Si system that the interfacial energetics are governed not by the commonly invoked electrolyte-induced pinch-off effect, but rather by a dipolemediated modulation of the effective work function of the EC/ SC interface driven by H<sub>2</sub> and O<sub>2</sub> adsorption. We show that these local chemical interactions dynamically alter the barrier height at the EC/SC interface, enabling a tunable transition between Ohmic and rectifying behavior. Our results establish that photovoltage in these systems emerges from a synergy between surface chemistry, interfacial oxide tunneling, and nonidealities at the junction. We provided a quantitative framework that demystifies the complex interfacial physics of nanostructured photoelectrodes and clarifies the mechanisms impacting charge transfer. Overall, the insights gained from this

study contribute to a deeper understanding of nanostructured photoelectrocatalysts and provides design principles for optimizing performance in practical devices.

### METHODS

**Sample Fabrication.** Boron doped (p-type, resistivity 10–20 Ohm-cm, (100)-oriented, 525 um thick, single-side polished) and phosphorus doped (n<sup>+</sup>-type, resistivity 0.001–0.005 Ohm-cm, (100)-oriented, 525  $\mu$ m thick, single-side polished) Si wafers were purchased from Addison Engineering. The Si wafers were hand-diced to 12 × 12 mm square pieces for all measurements.

Si pieces were cleaned using a hot piranha solution (3/1 by volume concentrated aqueous  $H_2SO_4/30\%$  aqueous  $H_2O_2$ ) for 15 min and etched in buffered hydrofluoric acid (BHF) for 2 min, followed by copious rinsing in DI water. The unpolished back-side of the wafer piece was scratched using a diamond tip scribe, excess silicon dust was removed, and gallium—indium eutectic paint (Alfa Aesar, 99.99%) was applied to the scratched area to ensure an Ohmic contact. The prepared wafer pieces were then housed in a custom 3-D printed electrode with an O-ring and a well-defined aperture of 0.459 cm<sup>2</sup> exposed to the electrolyte. The back contact was pressed against a copper plate.

For np-Pt/p-Si samples, Pt was (photo)electrodeposited on wafer pieces using a solution of 3 mM K<sub>2</sub>PtCl<sub>4</sub> (Sigma-Aldrich, 99.99%) and 0.5 M NaCl (Sigma-Aldrich). The pH of the solution was adjusted to 3.5 with 0.1 M HCl. The solution was then sonicated for 30 min and magnetically stirred for 15 min before and during electrodeposition. A single-junction Ag/AgCl (3 M KCl) reference electrode (Pine Research, FODR-0021) and platinum wire were placed in the electrodeposition solution. The positions of the beaker and the reference and counter electrodes were kept constant from sample to sample. The sample was illuminated at ~1-sun illumination. Ag/AgCl reference was not exposed to illumination to prevent degradation. Once the electrode was submerged in the electrodeposition solution, electrochemical impedance spectroscopy (EIS) was used on each sample to evaluate the overall resistance, which includes the solution resistance and the resistivity from the wafers. Pt was electrodeposited by running 6 consecutive linear sweep voltammograms (LSV) between 0.2 V to -0.8 V vs Ag/AgCl. Scan rate during electrodeposition was 25 mV s<sup>-1</sup>. The sample was then rinsed with DI water and immediately tested electrochemically.

For np-Pt@CrO $_x$ /p-Si samples, an electrodeposition solution of 0.1 M K $_2$ CrO $_4$  (Sigma-Aldrich) in 0.1 M KOH was prepared. Hg/HgO and graphite rod were used as reference and counter electrodes, respectively. CrO $_x$  was (photo)electrodeposited at a constant applied potential of -1.5 V vs Hg/HgO for 120 s under  $\sim$ 1-sun illumination. The sample was promptly taken out of the solution, rinsed with DI water and immediately tested electrochemically.

For pf-Pt/p-Si samples, Si pieces were cleaned and etched as before and were promptly taken to an electron-beam evaporation chamber (Angstrom Engineering EvoVac). Pt was e-beam evaporated (base pressure < 3  $\times$  10 $^{-6}$  Torr) on Si pieces at a rate of 1 Å s $^{-1}$  to a target thickness of 100 Å which was monitored by a quartz crystal microbalance.

Details on the fabrication of pf-Pt/Ti/HfO<sub>2</sub>/p-Si can be found in our prior work.<sup>33</sup> In short, cleaned and etched wafers were taken directly to a Veeco Fiji Atomic Layer Deposition tool and placed under vacuum. The samples were heated to 250 °C. Tetrakis-(dimethylamino)hafnium (TDMAH) was pulsed as the hafnium (Hf) precursor, followed by a pulse of water vapor. ALD was run for 15 cycles. After the ALD process was completed, samples were taken to the same e-beam evaporation chamber (Angstrom Engineering EvoVac). Samples were placed under  $4 \times 10^{-6}$  Torr vacuum and metals were deposited sequentially at a rate of 1 Å/s without breaking vacuum. Each metal film (Ti and Pt) was ~10 nm thick (see Figure S8 for cross-sectional STEM).

 $ss-Pt/SiO_x/p-Si$  and ss-Pt/p-Si were fabricated for dry solid-state measurements. Hand-diced Si pieces were cleaned as before using a fresh piranha solution (3/1 by volume concentrated aqueous  $H_2SO_4/$ 

30% aqueous  $\rm H_2O_2$ ) for 15 min and etched in fresh buffered hydrofluoric acid (BHF) for 2 min, followed by copious rinsing in DI water. For pf-Pt/SiO<sub>x</sub>/p-Si samples, SiO<sub>x</sub> was grown by immersing the cleaned and etched pieces in 68% HNO<sub>3</sub> at 120 °C for 10 min on a hot plate. <sup>74</sup> Pieces were then taken to the e-beam evaporation chamber (Angstrom Engineering EvoVac) and were shadow masked with Kapton tape to define a rectangular area at the center of the piece for metal deposition. The side and edges of the sample were also taped to minimize shunt pathways. Pt was e-beam evaporated at a base pressure < 3  $\times$  10 $^{-6}$  Torr with a rate of 2 Å s $^{-1}$  until a target thickness of 400 Å was reached.

**Electrochemical Testing.** All electrochemical measurements were taken with a Gamry Instruments Reference 3000 potentiostat (Figure S14a). For all photoelectrochemical HER experiments, the back side of the samples were scratched and painted with gallium—indium eutectic paint to ensure an Ohmic back contact. The samples were then pressed against a Cu plate and housed in a 3D-printed electrode. The illuminated area and the area exposed to the electrolyte were defined by an O-ring with an area of 0.4591 cm², and the current was normalized to this geometric area. All electrochemical experiments were performed using a three-electrode setup in a square quartz beaker.

For CV and OCV measurements, a 0.1 m KOH electrolyte was prepared using 45 wt % KOH (Sigma-Aldrich) and was sonicated for 15 min. Samples were illuminated using a 300 W UV 16S-Series Solar Simulator (Solar Light Company) with an AM 1.5 G filter. Light intensity was calibrated to 100 mW cm<sup>-2</sup> (or 1-sun) using a thermopile detector (Newport Corporation). p-type samples were illuminated during HER measurements while n+-type and FTO samples were tested in the dark. A Pt wire counter electrode and a Hg/HgO (Pine Research, RREF0038) reference electrode were used to complete the three-electrode setup. Cyclic voltammetry was conducted at a scan rate of 50 mV  $\rm s^{-1}$  unless otherwise stated. Recorded voltages were converted to RHE by calibrating a Hg/HgO reference electrode in a H<sub>2</sub>-saturated 0.1 M KOH solution with a Pt wire. All electrochemical current density-voltage data reported were fully IR-corrected using the solution resistance determined through EIS. The tested samples were rinsed with DI water and stored for further SEM and STEM analysis.

**Solid-State Electrical Measurements.** ss-Pt/SiO<sub>x</sub>/p-Si and ss-Pt/p-Si solid-state samples were also electrically characterized under dry conditions (Figure S14b). As before, unpolished back-side of the sample pieces were scratched using a diamond tip scribe, excess silicon dust was removed, and gallium—indium eutectic paint was applied to the scratched area to ensure an Ohmic contact.

Solid-state current-voltage (I-V) and impedance spectroscopy measurements were taken with a Gamry potentiostat. The back side of the sample was pressed on a double-sided Cu tape that was affixed on a microscope slide for structural support. Working electrode lead was connected to the Cu tape. A tungsten (W) probe (Form Factor, PTT-12/4-25) was mounted on a probe holder and the probe tip was made to gently contact the Pt layer on top of the sample. Reference and counter electrode leads were shorted and connected to the W probe holder. The thick Pt layer (~40 nm) prevented the probe from scratching down to the Pt film. The movement of the probe while contacting the sample was minimized. Optical microscope images showed no large pinholes and defects on the surface after contacting the probe. Gas flow on the sample was maintained by flooding pure H<sub>2</sub> and O<sub>2</sub> through a glass needle, monitored with a VWR mass flow controller. Some solid-state measurements were performed in a N2-purged glovebox (Vacuum Company OmniLab) to limit the  $O_2$  concentration in the environment.

Solid-state impedance spectroscopy measurements were performed with 0.1 V intervals between -0.5 V and -1.0 V with a frequency range of 1000-100 000 Hz and an AC voltage of 10 rms mV. Each impedance measurement was fit to an equivalent circuit to determine the space charge capacitance needed for the Mott–Schottky plots (see Supporting Information for details). Four point probe measurements were performed with a Four Dimensions 280DI instrument to determine the resistivity of wafers.

Sample Characterization. Scanning electron microscopy (SEM) was performed using the Thermo Fisher Nova 200 Nanolab with an accelerating voltage of 5 kV. Nanoparticle size, size distribution, and coverage were analyzed using IMAGEJ software. Scanning transmission electron microscopy (STEM) samples were prepared using a focused ion-beam (FIB) milling apparatus on the TFS Nova 200 Nanolab. STEM was performed with the Thermo Fisher Talos F200X G2 and also to gather energy dispersive X-ray spectroscopy (EDS) maps. Thermo Fisher Spectra 300 was sometimes used to take ultrahigh resolution images. Interfacial oxide thicknesses were measured using high-resolution STEM imaging where the Pt/SiO<sub>x</sub>/ p-Si interfaces were marked by changes in contrast and atomic lattice structure. The thicknesses were determined by analyzing several points across samples using the IMAGEJ software. X-ray photoelectron spectroscopy (XPS) measurements were performed using Kratos Axis Supra+. The C 1s peaks were aligned to 284.6 eV.

### ASSOCIATED CONTENT

# Supporting Information

The Supporting Information is available free of charge at https://pubs.acs.org/doi/10.1021/jacs.5c07369.

Additional details on sample fabrication; additional sample characterization; stability testing; impedance spectroscopy and Mott—Schottky analysis; parameter extraction methodologies; discussion of alternative dipole-mediated mechanisms; summary of experimental and modeling parameters; theory and details of the finite element model; additional simulation results (PDF)

#### AUTHOR INFORMATION

## **Corresponding Author**

Suljo Linic — Department of Chemical Engineering, University of Michigan, Ann Arbor, Michigan 48109, United States; Catalysis Science and Technology Institute, University of Michigan, Ann Arbor, Michigan 48109, United States; orcid.org/0000-0003-2153-6755; Email: linic@umich.edu

#### **Authors**

Ahmet Sert — Department of Chemical Engineering, University of Michigan, Ann Arbor, Michigan 48109, United States; Catalysis Science and Technology Institute, University of Michigan, Ann Arbor, Michigan 48109, United States; orcid.org/0000-0003-2802-3485

Aarti Mathur — Department of Chemical Engineering, University of Michigan, Ann Arbor, Michigan 48109, United States; Catalysis Science and Technology Institute, University of Michigan, Ann Arbor, Michigan 48109, United States

Complete contact information is available at: https://pubs.acs.org/10.1021/jacs.5c07369

#### **Notes**

The authors declare no competing financial interest.

# ACKNOWLEDGMENTS

The authors acknowledge support from the U.S. Department of Energy, Office of Basic Energy Sciences, Division of Chemical Sciences (DE-SC0021362). The authors also thank Michigan Center for Materials Characterization  $(MC^2)$  and Lurie Nanofabrication Facility (LNF) staff for technical assistance.

#### REFERENCES

- (1) Walter, M. G.; Warren, E. L.; McKone, J. R.; Boettcher, S. W.; Mi, Q.; Santori, E. A.; Lewis, N. S. Solar Water Splitting Cells. *Chem. Rev.* **2010**, *110* (11), 6446–6473.
- (2) Laskowski, F. A. L.; Oener, S. Z.; Nellist, M. R.; Gordon, A. M.; Bain, D. C.; Fehrs, J. L.; Boettcher, S. W. Nanoscale Semiconductor/Catalyst Interfaces in Photoelectrochemistry. *Nat. Mater.* **2020**, *19* (1), 69–76.
- (3) Hemmerling, J. R.; Mathur, A.; Linic, S. Characterizing the Geometry and Quantifying the Impact of Nanoscopic Electrocatalyst/Semiconductor Interfaces under Solar Water Splitting Conditions. *Adv. Energy Mater.* **2022**, *12* (11), 2103798.
- (4) Takata, T.; Jiang, J.; Sakata, Y.; Nakabayashi, M.; Shibata, N.; Nandal, V.; Seki, K.; Hisatomi, T.; Domen, K. Photocatalytic Water Splitting with a Quantum Efficiency of Almost Unity. *Nature* **2020**, *581* (7809), 411–414.
- (5) Mei, B.; Han, K.; Mul, G. Driving Surface Redox Reactions in Heterogeneous Photocatalysis: The Active State of Illuminated Semiconductor-Supported Nanoparticles during Overall Water-Splitting. ACS Catal. 2018, 8 (10), 9154–9164.
- (6) Hemmerling, J. R.; Mathur, A.; Linic, S. Design Principles for Efficient and Stable Water Splitting Photoelectrocatalysts. *Acc. Chem. Res.* **2021**, *54* (8), 1992–2002.
- (7) Zhang, Z.; Yates, J. T. Band Bending in Semiconductors: Chemical and Physical Consequences at Surfaces and Interfaces. *Chem. Rev.* **2012**, *112* (10), 5520–5551.
- (8) Mathur, A.; Sert, A.; Linic, S. Common Misconceptions in the Analysis of Critical Figures of Merit for Functioning Electrocatalyst/Semiconductor Photoelectrocatalysts under Solar Water-Splitting Conditions. ACS Energy Lett. 2024, 9, 4136–4146.
- (9) Takanabe, K. Photocatalytic Water Splitting: Quantitative Approaches toward Photocatalyst by Design. ACS Catal. 2017, 7 (11), 8006–8022.
- (10) Dominey, R. N.; Lewis, N. S.; Bruce, J. A.; Bookbinder, D. C.; Wrighton, M. S. Improvement of Photoelectrochemical Hydrogen Generation by Surface Modification of P-Type Silicon Semiconductor Photocathodes. *J. Am. Chem. Soc.* **1982**, *104* (2), 467–482.
- (11) Maier, C. Hydrogen Evolution on Platinum-Coated p-Silicon Photocathodes. *Int. J. Hydrogen Energy* **1996**, 21 (10), 859–864.
- (12) Szklarczyk, M.; Bockris, J. O. Photoelectrocatalysis and Electrocatalysis on P-Silicon. J. Phys. Chem. 1984, 88 (9), 1808–1815.
- (13) Huang, Z.; McKone, J. R.; Xiang, C.; Grimm, R. L.; Warren, E. L.; Spurgeon, J. M.; Lewerenz, H.-J.; Brunschwig, B. S.; Lewis, N. S. Comparison between the Measured and Modeled Hydrogen-Evolution Activity of Ni- or Pt-Coated Silicon Photocathodes. *Int. J. Hydrogen Energy* **2014**, *39* (28), 16220–16226.
- (14) McKone, J. R.; Warren, E. L.; Bierman, M. J.; Boettcher, S. W.; Brunschwig, B. S.; Lewis, N. S.; Gray, H. B. Evaluation of Pt, Ni, and Ni–Mo Electrocatalysts for Hydrogen Evolution on Crystalline Si Electrodes. *Energy Environ. Sci.* **2011**, *4* (9), 3573.
- (15) Hernley, P. A.; Chavez, S. A.; Quinn, J. P.; Linic, S. Engineering the Optical and Catalytic Properties of Co-Catalyst/Semiconductor Photocatalysts. *ACS Photonics* **2017**, *4* (4), 979–985.
- (16) Labrador, N. Y.; Li, X.; Liu, Y.; Tan, H.; Wang, R.; Koberstein, J. T.; Moffat, T. P.; Esposito, D. V. Enhanced Performance of Si MIS Photocathodes Containing Oxide-Coated Nanoparticle Electrocatalysts. *Nano Lett.* **2016**, *16* (10), 6452–6459.
- (17) Lombardi, I.; Marchionna, S.; Zangari, G.; Pizzini, S. Effect of Pt Particle Size and Distribution on Photoelectrochemical Hydrogen Evolution by P-Si Photocathodes. *Langmuir* **2007**, 23 (24), 12413–12420.
- (18) Jiang, J.; Huang, Z.; Xiang, C.; Poddar, R.; Lewerenz, H.; Papadantonakis, K. M.; Lewis, N. S.; Brunschwig, B. S. Nanoelectrical and Nanoelectrochemical Imaging of Pt/p-Si and Pt/p <sup>+</sup> -Si Electrodes. *ChemSuschem* **2017**, *10* (22), 4657–4663.
- (19) Nakato, Y.; Tsubomura, H. Silicon Photoelectrodes Modified with Ultrafine Metal Islands. *Electrochim. Acta* **1992**, *37* (5), 897–907.
- (20) Fabre, B.; Li, G.; Gouttefangeas, F.; Joanny, L.; Loget, G. Tuning the Photoelectrocatalytic Hydrogen Evolution of Pt-

- Decorated Silicon Photocathodes by the Temperature and Time of Electroless Pt Deposition. *Langmuir* **2016**, 32 (45), 11728–11735.
- (21) Nunez, P.; Cabán-Acevedo, M.; Yu, W.; Richter, M. H.; Kennedy, K.; Villarino, A. M.; Brunschwig, B. S.; Lewis, N. S. Origin of the Electrical Barrier in Electrolessly Deposited Platinum Nanoparticles on P-Si Surfaces. *J. Phys. Chem. C* **2021**, *125* (32), 17660–17670.
- (22) Kaufman, A. J.; Krivina, R. A.; Shen, M.; Boettcher, S. W. Controlling Catalyst—Semiconductor Contacts: Interfacial Charge Separation in p-InP Photocathodes. *ACS Energy Lett.* **2022**, *7* (1), 541–549.
- (23) Chen, Y.; Xiang, C.; Lin, M. Performance Assessment of Photoelectrochemical CO<sub>2</sub> Reduction Photocathodes with Patterned Electrocatalysts: A Multi-Physical Model-Based Approach. *Energy Environ. Sci.* **2024**, *17* (9), 3032–3041.
- (24) Pan, Z.; Yanagi, R.; Wang, Q.; Shen, X.; Zhu, Q.; Xue, Y.; Röhr, J. A.; Hisatomi, T.; Domen, K.; Hu, S. Mutually-Dependent Kinetics and Energetics of Photocatalyst/Co-Catalyst/Two-Redox Liquid Junctions. *Energy Environ. Sci.* **2020**, *13* (1), 162–173.
- (25) Nakato, Y.; Ueda, K.; Yano, H.; Tsubomura, H. Effect of Microscopic Discontinuity of Metal Overlayers on the Photovoltages in Metal-Coated Semiconductor-Liquid Junction Photoelectrochemical Cells for Efficient Solar Energy Conversion. *J. Phys. Chem.* **1988**, 92 (8), 2316–2324.
- (26) Tung, R. T. Electron Transport of Inhomogeneous Schottky Barriers. *Appl. Phys. Lett.* **1991**, *58* (24), 2821–2823.
- (27) Rossi, R. C.; Tan, M. X.; Lewis, N. S. Size-Dependent Electrical Behavior of Spatially Inhomogeneous Barrier Height Regions on Silicon. *Appl. Phys. Lett.* **2000**, *77* (17), 2698–2700.
- (28) King, A. J.; Weber, A. Z.; Bell, A. T. Understanding Photovoltage Enhancement in Metal–Insulator Semiconductor Photoelectrodes with Metal Nanoparticles. *ACS Appl. Mater. Interfaces* **2024**, *16* (28), 36380–36391.
- (29) Hill, J. C.; Landers, A. T.; Switzer, J. A. An Electrodeposited Inhomogeneous Metal–Insulator–Semiconductor Junction for Efficient Photoelectrochemical Water Oxidation. *Nat. Mater.* **2015**, *14* (11), 1150–1155.
- (30) Oh, K.; Mériadec, C.; Lassalle-Kaiser, B.; Dorcet, V.; Fabre, B.; Ababou-Girard, S.; Joanny, L.; Gouttefangeas, F.; Loget, G. Elucidating the Performance and Unexpected Stability of Partially Coated Water-Splitting Silicon Photoanodes. *Energy Environ. Sci.* **2018**, *11* (9), 2590–2599.
- (31) Lin, F.; Boettcher, S. W. Adaptive Semiconductor/Electrocatalyst Junctions in Water-Splitting Photoanodes. *Nat. Mater.* **2014**, 13 (1), 81–86.
- (32) Heller, A. Hydrogen-Evolving Solar Cells. *Science* **1984**, 223 (4641), 1141–1148.
- (33) Quinn, J.; Hemmerling, J.; Linic, S. Guidelines for Optimizing the Performance of Metal–Insulator–Semiconductor (MIS) Photoelectrocatalytic Systems by Tuning the Insulator Thickness. *ACS Energy Lett.* **2019**, 4 (11), 2632–2638.
- (34) King, A. J.; Weber, A. Z.; Bell, A. T. Theory and Simulation of Metal—Insulator—Semiconductor (MIS) Photoelectrodes. *ACS Appl. Mater. Interfaces* **2023**, *15* (19), 23024–23039.
- (35) Fajardo, A. M.; Lewis, N. S. Rate Constants for Charge Transfer Across Semiconductor-Liquid Interfaces. *Science* **1996**, 274 (5289), 969–972.
- (36) Gerischer, H. Electron-Transfer Kinetics of Redox Reactions at the Semiconductor/Electrolyte Contact. A New Approach. *J. Phys. Chem.* **1991**, 95 (3), 1356–1359.
- (37) Bard, A. J.; Faulkner, L. R.; White, H. S. *Electrochemical Methods: Fundamentals and Applications*, 3nd ed.; John Wiley & Sons, Inc: New York, 2022.
- (38) Digdaya, I. A.; Trzesniewski, B. J.; Adhyaksa, G. W. P.; Garnett, E. C.; Smith, W. A. General Considerations for Improving Photovoltage in Metal–Insulator–Semiconductor Photoanodes. *J. Phys. Chem. C* 2018, 122 (10), 5462–5471.

- (39) Jung, J.-Y.; Yu, J.-Y.; Lee, J.-H. Dynamic Photoelectrochemical Device with Open-Circuit Potential Insensitive to Thermodynamic Voltage Loss. *J. Phys. Chem. Lett.* **2018**, *9* (18), 5412–5418.
- (40) Zhao, T.; Yanagi, R.; Xu, Y.; He, Y.; Song, Y.; Yang, M.; Hu, S. A Coating Strategy to Achieve Effective Local Charge Separation for Photocatalytic Coevolution. *Proc. Natl. Acad. Sci. U. S. A.* **2021**, *118* (7), No. e2023552118.
- (41) Holewinski, A.; Linic, S. Elementary Mechanisms in Electrocatalysis: Revisiting the ORR Tafel Slope. *J. Electrochem. Soc.* **2012**, 159 (11), H864–H870.
- (42) Liu, E.; Li, J.; Jiao, L.; Doan, H. T. T.; Liu, Z.; Zhao, Z.; Huang, Y.; Abraham, K. M.; Mukerjee, S.; Jia, Q. Unifying the Hydrogen Evolution and Oxidation Reactions Kinetics in Base by Identifying the Catalytic Roles of Hydroxyl-Water-Cation Adducts. *J. Am. Chem. Soc.* **2019**, *141* (7), 3232–3239.
- (43) Dix, S. T.; Linic, S. In-Operando Surface-Sensitive Probing of Electrochemical Reactions on Nanoparticle Electrocatalysts: Spectroscopic Characterization of Reaction Intermediates and Elementary Steps of Oxygen Reduction Reaction on Pt. J. Catal. 2021, 396, 32—39
- (44) Bard, A. J.; Bocarsly, A. B.; Fan, F. R. F.; Walton, E. G.; Wrighton, M. S. The Concept of Fermi Level Pinning at Semiconductor/Liquid Junctions. Consequences for Energy Conversion Efficiency and Selection of Useful Solution Redox Couples in Solar Devices. J. Am. Chem. Soc. 1980, 102 (11), 3671–3677.
- (45) Bocarsly, A. B.; Bookbinder, D. C.; Dominey, R. N.; Lewis, N. S.; Wrighton, M. S. Photoreduction at Illuminated P-Type Semiconducting Silicon Photoelectrodes. Evidence for Fermi Level Pinning. J. Am. Chem. Soc. 1980, 102 (11), 3683–3688.
- (46) Madou, M.; Brondeel, P.; Gomes, W. P.; Hanselaer, P.; Cardon, F. Investigation on Photoelectrochemical Cells Based upon Silicon/Methanol Interfaces. Part 2: P-Type Si. *Sol. Energy Mater.* **1982**, 7 (1), 33–42.
- (47) Lewerenz, H. J. Surface States and Fermi Level Pinning at Semiconductor/Electrolyte Junctions. *J. Electroanal. Chem.* **1993**, 356 (1–2), 121–143.
- (48) Sze, S. M.; Ng, K. K. Physics of Semiconductor Devices; John Wiley & Sons, 2006.
- (49) Chazalviel, J.-N. Schottky Barrier Height and Reverse Current of the N-Si-Electrolyte Junction. Surf. Sci. 1979, 88 (1), 204–220.
- (50) Maeda, K.; Teramura, K.; Lu, D.; Saito, N.; Inoue, Y.; Domen, K. Noble-Metal/Cr  $_2$  O  $_3$  Core/Shell Nanoparticles as a Cocatalyst for Photocatalytic Overall Water Splitting. *Angew. Chem., Int. Ed.* **2006**, 45 (46), 7806–7809.
- (51) Yoshida, M.; Takanabe, K.; Maeda, K.; Ishikawa, A.; Kubota, J.; Sakata, Y.; Ikezawa, Y.; Domen, K. Role and Function of Noble-Metal/Cr-Layer Core/Shell Structure Cocatalysts for Photocatalytic Overall Water Splitting Studied by Model Electrodes. *J. Phys. Chem. C* **2009**, *113* (23), 10151–10157.
- (52) Qureshi, M.; Shinagawa, T.; Tsiapis, N.; Takanabe, K. Exclusive Hydrogen Generation by Electrocatalysts Coated with an Amorphous Chromium-Based Layer Achieving Efficient Overall Water Splitting. ACS Sustainable Chem. Eng. 2017, 5 (9), 8079–8088.
- (53) Aspnes, D. E.; Heller, A. Photoelectrochemical Hydrogen Evolution and Water Photolyzing Semiconductor Suspensions: Properties of Platinum Group Metal Catalyst-Semiconductor Contacts in Air and in Hydrogen. J. Phys. Chem. 1983, 87 (24), 4919—4929.
- (54) Card, H. C.; Rhoderick, E. H. Studies of Tunnel MOS Diodes I. Interface Effects in Silicon Schottky Diodes. *J. Phys. Appl. Phys.* **1971**, 4 (10), 1589–1601.
- (55) Bond, G. C. Catalysis by Metals; Academic Press: New York, 1962
- (56) Yamamoto, N.; Tonomura, S.; Matsuoka, T.; Tsubomura, H. A Study on a Palladium-Titanium Oxide Schottky Diode as a Detector for Gaseous Components. *Surf. Sci.* **1980**, 92 (2–3), 400–406.
- (57) Collins, D. M.; Spicer, W. E. The Adsorption of CO, O2, and H2 on Pt. Surf. Sci. 1977, 69 (1), 114–132.

- (58) Netzer, F. P.; Wille, R. A. Adsorption Studies on a Stepped Pt(111) Surface: O2, CO, C2H4, C2N2. Surf. Sci. 1978, 74 (3), 547–567.
- (59) Derry, G. N.; Ross, P. N. A Work Function Change Study of Oxygen Adsorption on Pt(111) and Pt(100). *J. Chem. Phys.* **1985**, 82 (6), 2772–2778.
- (60) Ruths, P. F.; Ashok, S.; Fonash, S. J.; Ruths, J. M. A Study of Pd/Si MIS Schottky Barrier Diode Hydrogen Detector. *IEEE Trans. Electron Devices* **1981**, 28 (9), 1003–1009.
- (61) Kobayashi, H.; Kogetsu, Y.; Nakato, Y. Mechanism of Hydrogen Sensing by Platinum/silicon Oxide/silicon MIS Tunneling Diodes. *Surf. Sci.* **1994**, *306* (1–2), 69–80.
- (62) Christmann, K.; Ertl, G.; Pignet, T. Adsorption of Hydrogen on a Pt(111) Surface. Surf. Sci. 1976, 54 (2), 365–392.
- (63) Kobayashi, H.; Kishimoto, K.; Nakato, Y. Reactions of Hydrogen at the Interface of Palladium-Titanium Dioxide Schottky Diodes as Hydrogen Sensors, Studied by Workfunction and Electrical Characteristic Measurements. Surf. Sci. 1994, 306 (3), 393–405.
- (64) Norton, P. R.; Goodale, J. W. Hydrogen on Pt(111) Studied by Dynamic Measurements of the Work Function. *Solid State Commun.* 1979, 31 (4), 223–227.
- (65) Ponpon, J. P.; Siffert, P. Role of Oxygen in the Mechanism of Formation of Schottky Diodes. *J. Appl. Phys.* **1978**, *49* (12), 6004–6011
- (66) Ekedahl, L.-G.; Eriksson, M.; Lundström, I. Hydrogen Sensing Mechanisms of Metal–Insulator Interfaces. *Acc. Chem. Res.* **1998**, *31* (5), 249–256.
- (67) Ebisuzaki, Y.; Kass, W. J.; O'Keeffe, M. Solubility and Diffusion of Hydrogen and Deuterium in Platinum. *J. Chem. Phys.* **1968**, 49 (8), 3329–3332.
- (68) Schmiedl, R.; Demuth, V.; Lahnor, P.; Godehardt, H.; Bodschwinna, Y.; Harder, C.; Hammer, L.; Strunk, H.-P.; Schulz, M.; Heinz, K. Oxygen Diffusion through Thin Pt Films on Si(100). *Appl. Phys. A* **1996**, *62* (3), 223–230.
- (69) Ponpon, J. P.; Siffert, P. Further Results on the Aging of Silicon Schottky Diodes: Influence of the Metal. *J. Appl. Phys.* **1979**, *50* (7), 5050–5051.
- (70) Yamamoto, N.; Tonomura, S.; Matsuoka, T.; Tsubomura, H. Effect of Various Substrates on the Hydrogen Sensitivity of Palladium-Semiconductor Diodes. *J. Appl. Phys.* **1981**, *52* (10), *6227–6230*.
- (71) Ingram, D. B.; Linic, S. First-Principles Analysis of the Activity of Transition and Noble Metals in the Direct Utilization of Hydrocarbon Fuels at Solid Oxide Fuel Cell Operating Conditions. *J. Electrochem. Soc.* **2009**, *156* (12), B1457.
- (72) Heller, A.; Aharon-Shalom, E.; Bonner, W. A.; Miller, B. Hydrogen-Evolving Semiconductor Photocathodes: Nature of the Junction and Function of the Platinum Group Metal Catalyst. *J. Am. Chem. Soc.* **1982**, *104* (25), 6942–6948.
- (73) Hemmerling, J.; Quinn, J.; Linic, S. Quantifying Losses and Assessing the Photovoltage Limits in Metal–Insulator–Semiconductor Water Splitting Systems. *Adv. Energy Mater.* **2020**, *10* (12), 1903354.
- (74) Kobayashi Asuha, H.; Maida, O.; Takahashi, M.; Iwasa, H. Nitric Acid Oxidation of Si to Form Ultrathin Silicon Dioxide Layers with a Low Leakage Current Density. *J. Appl. Phys.* **2003**, *94* (11), 7328–7335.

